Engineering Fracture Mechanics 252 (2021) 107842

Contents lists available at ScienceDirect

Engineering Fracture Mechanics

journal homepage: www.elsevier.com/locate/engfracmech

Side-grooved Charpy impact testing: Assessment of splitting and fracture properties of high-toughness plate steels

F. Di Gioacchino [a,*], E. Lucon [b], E.B. Mitchell [a], K.D. Clarke [a], D.K. Matlock [a]

[a] ASPPRC, Department of Metallurgical and Materials Engineering, Colorado School of Mines, 1500 Illinois St., Golden, CO, USA
[b] Advanced Chemicals and Materials Division, National Institute for Standards and Technology (NIST), 325 Broadway, Boulder, CO, USA

ARTICLE INFO

Keywords:
Delamination
Fracture toughness
Impact testing
Pipeline steels
Side grooves

ABSTRACT

The fracture properties and susceptibility to crack-divider delamination (or splitting) of three commercially produced high-toughness X70 pipeline steels are evaluated with Charpy impact test samples modified to incorporate side grooves. Temperature-dependent impact data are compared with standard Charpy V–notch (CVN) and drop weight tear test data (DWTT). It is shown that the modified geometry prevents the accumulation of plastic deformation at upper shelf energy temperatures and improves the accuracy of impact properties measurements. It also promotes splitting, mirroring the splitting behavior assessed with DWTT samples. To demonstrate the effects of splitting on fracture characteristics and impact energies, steels with similar tensile properties but different splitting susceptibilities are considered. Splitting severity is maximum close to the ductile–brittle transition temperature. However, the effect of splitting on impact energy is minimum at such temperature, as this type of delamination increases energy absorption at lower temperatures and decreases it by a similar extent at higher temperatures. This finding is discussed by examination of force–displacement curves from the instrumented impact tests.

1. Introduction

The high costs of full-scale pipeline burst tests have incentivized the use of laboratory impact testing methods, most notably the drop-weight tear test (DWTT) and the Charpy V-notch (CVN) test, to assess the suitability of plate steels for pipeline manufacture. These impact test methods have been successfully employed to evaluate dynamic crack arrestability in low-grade plate steels [1]. However, limitations in the applicability of both DWTT and CVN methods have recently emerged, following the development of high-toughness plate steels with refined microstructures produced by thermomechanical controlled processing (TMCP). DWTT results on these steels at transitional temperatures often exhibit high variability in absorbed energies and mixed-mode (brittle/ductile) fracture surfaces, referred to as abnormal fracture, that leads to invalid tests according to API standards [2,3]. In CVN testing at high temperatures, the combination of high fracture toughness and the weakening of stress triaxiality associated with the reduced thickness of the standard CVN sample geometry often causes extensive plastic deformation, limited cracking before the test piece exits the anvil, and overestimation of crack arrestability [4].

In an effort to utilize small-scale samples for testing high toughness steels, as summarized in Table 1 several investigators have employed side grooves in standard and sub-sized CVN samples to induce stress states that approximate plane strain conditions [4–21]. For each citation, tabulated information includes details of the sample geometry, a brief description of the focus of the study, the steel

* Corresponding author.
E-mail address: fdigioacchino@mines.edu (F. Di Gioacchino).

https://doi.org/10.1016/j.engfracmech.2021.107842
Received 24 December 2020; Received in revised form 3 May 2021; Accepted 9 June 2021
Available online 15 June 2021
0013-7944/© 2021 Published by Elsevier Ltd.

Nomenclature

a ,b, c, d	Fitting parameters of the hyperbolic tangent function
E	Absorbed energy
S_r	Splitting ratio
T	Testing temperature
API	American Petroleum Institute
ASTM	American Society for Testing and Materials
CVN	Charpy V-notch
CVN-mod	Modified Charpy V-notch
DBTT	Ductile-to-brittle transition temperature
DWTT	Drop weight tear testing
EDM	Electric discharge machining
HTR	One half of the transition region
L, S, T	Longitudinal, short transverse, and transverse directions
MA	Martensite-austenite
TMCP	Thermomechanical controlled processing
USE	Upper shelf energy
X70-13.5	13.5 mm thick X70 plate material
X70-15.5	15.5 mm thick X70 plate material
X70-22	22 mm thick X70 plate material

alloy or alloys investigated, and any special imposed test conditions (*e.g.* deformation rate). These studies focused primarily on assessing transition temperatures, controlling crack geometry, evaluating crack initiation energies, or direct fracture toughness measurements on small samples. In comparison to standard CVN tests, several investigations showed that the presence of the side grooves caused upper shelf energy (USE) to decrease [7,10,11,14,15] and ductile-to-brittle transition temperature (DBTT) to increase [14,15]. These observations were attributed to the increase in stress triaxiality resulting from the lateral constraint imposed by the side grooves.

The increase of through-thickness tensile stresses in side-grooved samples may be expected to promote delamination on preferential fracture planes, *i.e.* planes with lowered resistance to fracture, that are oriented parallel to the rolling plane. Recent studies on fracture in pipeline steels [24–26] have shown that the susceptibility to delamination is an important material characteristic that must be assessed when considering the suitability of the newer high-toughness plate steels for pipeline applications. For example, Pyshmintsev *et al.* [25] performed full–scale burst tests on pipe sections produced from four X80 commercial steels, all of which met API 5L specifications for CVN and DWTT [27]. One steel exhibited extensive, unstable ductile crack growth and the presence of multiple fissures parallel to the plate surface, while ductile fracture in the other three steels was associated with normal shear fracture leading to crack arrest within a finite distance. These results highlight the importance of developing a laboratory test that focuses on toughness-related properties to assess the susceptibility of plate steels to delamination during ductile fracture.

Preferential fracture planes in plate steels may arise from variations in hot rolling schedules [28] due to a variety of causes including: compositional and microstructural banding [28–32], the development of crystallographic texture that includes alignment of {1 0 0} cleavage planes in bands parallel to the rolling plane in the {1 0 0} ⟨1 1 0⟩ texture [10,33–37], clustering of cube-oriented grains [38], grain boundary inclusions [39,40], and concentrations of high-angle grain boundaries [41]. The presence of preferential fracture planes leads to variations in fracture response that depend on crack growth direction, and thus sample orientations must be carefully selected to assess the fracture response of interest. As shown schematically in Fig. 1**(a)**, sample orientations in this manuscript are referenced to the conventionally accepted system [42] where the following coordinate system is used for plate steels to identify sample orientations and crack growth directions: L = longitudinal (parallel to rolling direction); T = transverse (parallel to the rolling plane and perpendicular to L), and S = short transverse (perpendicular to the rolling plane, and thus perpendicular to L). In CVN samples with length parallel to L and crack growth oriented in the through-thickness, *i.e.* short transverse, direction, S, (sample orientation referred to as L-S), as illustrated in Fig. 1**(b)**, delamination leads to crack growth out of the primary fracture plane, forcing the crack to reinitiate in the detached layers. This leads to crack growth known as “crack-arrester delamination” [43] and material response referred to as “delamination toughening” [44], which has been widely exploited to improve the performance of ceramics [45] and metals, including steels [46–51]. In contrast, samples machined with an L-T orientation led to fissures that propagated perpendicular to the main crack to create “crack-divider delamination” or “splitting”, as shown schematically in Fig. 1**(c).**

Characterization of splitting in plate steels is an important aspect in the assessment of pipeline performance, as this type of delamination mirrors that observed in full-scale pipeline burst tests [35]. However, the effects of splitting on the impact properties of plate steels measured on samples oriented to promote crack-divider type fracture are less evident than for crack-arrester conditions [52]. Reductions in ductile-to-brittle transition temperatures (DBTT) in crack divider (L-T) samples have been observed [39] and attributed to the development of plane stress states and localized plastic deformation in individual layers, resulting in decreases of DBTT analogous to shifts observed for the Charpy impact testing of samples with decreasing thickness [39]. By contrast, other studies have observed an increase in transition temperatures with splitting [53,54]. Furthermore, the specific effects of splitting on ductile

Table 1
Summary of experimental studies that have utilized side-grooved standard or sub-sized CVN samples to assess fracture properties of steels. Sample dimensions (all shown in mm) tabulated include: width, or distance between notched face and opposite face (W); thickness, or dimension perpendicular to the width and parallel to the notch (B); length, or largest dimension perpendicular to the notch (L); and side groove depth for each side (see Note 1 for comments on historical dimension designations).

Year	Material (Compositions in wt pct)	Purpose	B	W	L	Side groove depth	Side groove geometry/ machining	Notch Type	Ref.
1970	0.18C,0.8 Mn, 0.04Si	Modifying crack front geometry for slow-bend crack opening displacement (COD) tests	10	10	55	0.5. 0.75, or 1.0	Not specified	CVN	[5]
			12	10	55	1			
1975 Parts I & II	"Hyplus 29" plate steel 0.17C, 0.29Si, 1.54Mn, 0.1 V	Assessing modifications to CVN stress state via notch acuity and side grooves on crack nucleation and corresponding effect on toughness Evaluating effect of strain rates using slow bend testing of CVN samples on toughness parameters, lateral expansion, COD	12	10	55	1			
			14	10	55	2	Machined with Charpy V-notch broaching tool	CVN or slit with 0.15 radius	[14,15]
1978 & 1982	SAE-516–70 Steel 0.29C, 0.92Mn, 0.21Si	Determining fracture toughness from side grooved CVN samples in slow three-point bending and impact testing Determining transition temperatures; compared standard CVN data to fatigue precracked and side-grooved samples	10	10	55	1	1 mm radius or 1 mm V-notch	CVN or with fatigue precrack	[16,18]
1980	SA533B-1 Steel 0.23C, 1.55Mn, 0.24Si SA302B Steel 0.23C, 1.47Mn, 0.26Si	Determining fracture toughness from side grooved CVN samples with a single impact test	10–15	10	55	Up to 2.5	0.25 mm radius with 45° V-notch	CVN with fatigue precrack	[17]
1989 & 1990	ASTM A508 various heat treatments	For sample removal from nuclear reactors, comparing standard ASTM CVN samples with sub-sized; measured fracture toughness Determining shift in transition temperatures with sample geometry; utilized both slow bend and impact	4.83	4.83	12.7	0.49	Notch and side groove radius = 0.25 mm	CVN	[19,20]
1992 & 1994	A508CL3-A 0.14C, 1.29Mn, 0.27Si A508CL3-B 0.20C, 1.29Mn, 0.2Si BHW35 0-14C, 1.32Mn, 0.34Si	Determining the relationship between critical side-groove depth and fracture toughness	10	10	55	Up to 3	V-notch	CVN or with fatigue precrack	[6,21]

Year	Material (Compositions in wt pct)	Purpose	W	D	L	Side groove depth	Side groove geometry/ machining	Notch Type	Ref.
2000	ASTM A533B Class 1 steel	Summarizing multiple different tests; side-grooved tests used to measure % of shear transition temperature shift	3	4	27	0.3	Not specified	60° V-notch, 1 mm deep	[7]
2007	Nodular cast iron GJS-400	Validating 2D finite element analysis to model side-grooved CVN testing	10	10	55	1	Not specified	CVN with fatigue precrack	[8]
2013	X80 pipe-line steel	Determining fracture toughness and critical tearing modulus using special "constraint-modified" CVN sample	Note 2	10	55	1	EDM slits	EDM slit	[4]
			10	10	55	1			
2015 & 2019	Steel 45 ferrite-pearlite structural steel	Using side grooves to produce uniform crack front to assist in determining crack initiation energies from instrumented impact tests Evaluating fracture morphology to assess contributions of shear lips to measured impact properties	10	10	55	2	Same as Charpy V-notch	CVN	[9,13]
2016 & 2018	X70 pipe-line steel	Proposing a test for use with conventional (low-capacity) Charpy equipment to assess splitting susceptibility	12	10	55	1	EDM slits	CVN	[10,11]
2018	T200 (18Ni, 3Mo maraging steel) and X65 pipe-line steel	Evaluating standard and sub-sized geometries to obtain direct fracture mechanics data in instrumented impact tests	10	10	55	1	EDM slits	CVN; EDM slit; Fatigue precrack; saw cut	[12]

Note 1: Until the 2010 version of ISO 148:1 [22], the distance between the notched fact and the opposite face of the specimen was designated "height" (*h*), and the dimension perpendicular to the height that is aligned with the notch was designated "width" (*w*). In versions of ASTM E23 [23] up to 2012, the first dimension was termed "width" (*W*) and the second one was termed "thickness" (*T*).
Note 2: "Constraint modified" sample contains additional material (approximately 6 mm wide, 9 mm deep, and 20 mm long) integrally machined with and centered on each side of the sample, aligned with the surface containing the primary notch.

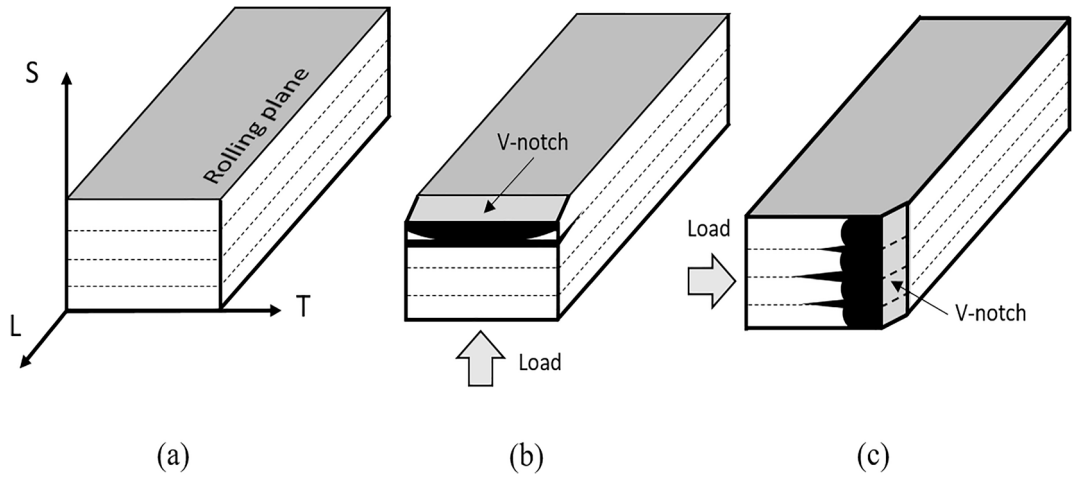

Fig. 1. Schematic drawings showing: (a) preferential fracture planes in a rolled plate along with the longitudinal (L), transverse (T) and short transverse (S) coordinate system used to identify CVN sample orientations; (b) CVN L-S orientation leading to crack-arrester delamination; and (c) CVN L-T orientation leading to crack-divider delamination or splitting.

fracture response at higher temperatures is still unclear [32,52]. For example, changing the orientation of the test pieces from T-L to L-T has been found to either increase or decrease impact energies and splitting at upper-shelf energy (USE) temperatures [39,50,55–58]. However, varying the sample orientation with respect to the rolling direction of a textured plate does not alter the splitting susceptibility of microstructurally–sensitive preferential fracture planes. For these textured plates, the degree of splitting therefore depends solely on the intensity of through-thickness tensile stresses, which may vary with the direction of impact with respect to the orientation-dependent yielding and strain hardening behavior of the material [32].

Recently, the side-grooved geometry adopted by Al-Jabr *et al.* [10,11] has been shown to enhance splitting of commercial X70 plate steels in comparison to results on standard CVN samples. In the present study, quantitative methods are used to assess the same modified geometry, here referred to as CVN-mod, as a suitable method to assess splitting and evaluate fracture properties of high toughness pipeline steels. Data are obtained for three X70 plate steels and used to provide direct comparisons with standard CVN and DWTT test results obtained previously for the same materials [59]. As two of the three X70 steels have similar tensile properties but significantly different splitting susceptibility, CVN-mod tests for these materials are separately compared to characterize the effect of splitting on impact energy at different testing temperatures.

2. Materials

Three commercial high-toughness X70 plates of 13.5, 15.5 and 22 mm thickness for which DWTT and CVN data are available [59] were selected for analysis. The nominal chemical compositions of the plate steels are given in Table 2**.** Details on the proprietary TMCP histories for each steel were unavailable. Fig. 2 shows light optical micrographs viewed in the transverse direction of the three steels taken at the quarter-depth positions in the plate cross sections [60]. The 13.5 mm and 15.5 mm thick plates in Fig. 2**(a) and 2(b)** exhibited fine polygonal ferrite microstructures. As detailed elsewhere, the microstructures included elongated grains close to the plate surfaces and nearly equiaxed grains along the centerlines [59]. The 13.5 mm thick plate also exhibited pearlite colonies that increased in number towards the centerline region of the plate. Fig. 2**(c)** shows that the 22 mm thick plate displayed a banded, ferrite/bainite microstructure with martensite-austenite (MA) constituents at the centerline [59,60]. However, while not quantified, based on the metallographic observations the amount of retained austenite was low, at a level interpreted to provide insignificant strengthening due to transformation to martensite during deformation.

Table 3 reports yield strength, ultimate tensile strength, and elongation at fracture values from quasi–static, room temperature testing of 5.6 mm thick tensile samples machined at centerline depth along the rolling (0°), diagonal (45°), and transverse (90°) directions [60]. Values determined for the 13.5 mm and 15.5 mm thick plates differ by less than 8%. This difference was found to be independent of the in-plane direction of loading so that the two plate materials displayed similar plastic anisotropy. Tensile strengths for the 22 mm thick plate material were lower than the corresponding values for the other two steels, and may reflect the effects of the

Table 2
Chemical Composition of the X70 Pipeline Steels in wt % (NR Indicates Not Reported) [60]

Plate thickness (mm)	C	Mn	Si	Cr	Al	Ni	S	P	Ti + Nb + V
22	0.040	1.62	0.23	0.16	0.03	NR	0.004	0.013	≤0.06
15.5	0.050	1.51	0.20	0.14	0.03	0.01	0.002	0.005	≤0.09
13.5	0.052	1.57	0.21	0.12	0.04	0.02	0.003	0.010	≤0.10

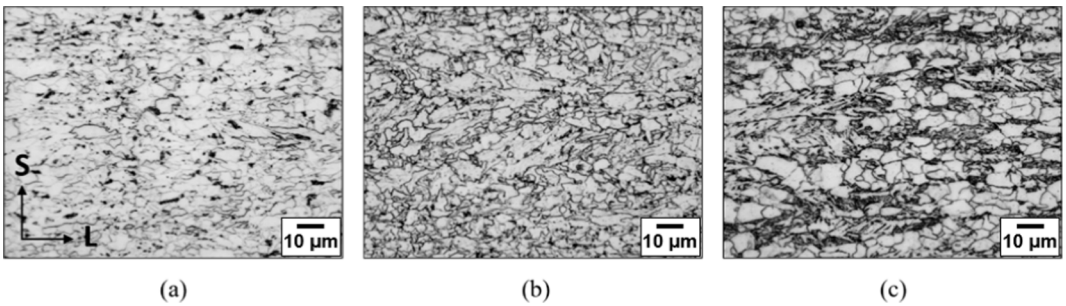

Fig. 2. Light optical micrographs taken at the quarter-depth positions in the plate cross sections of the experimental steel viewed in the transverse direction: (a) X70-13.5, (b) X70-15.5, and (c) X70-22 (2% nital etch).

Table 3
Tensile Properties of the Three Plate Materials Along the Rolling (RD), Diagonal (D), and Transverse Direction (TD) [60]

Plate thickness (mm)	Orientation	YS(MPa)	UTS(MPa)	YS/UTS	Elongation at fracture
13.5	RD	555	637	0.87	0.24
	D	532	626	0.85	0.26
	TD	596	676	0.88	0.23
15.5	RD	521	629	0.83	0.27
	D	525	609	0.86	0.30
	TD	549	635	0.87	0.26
22	RD	470	619	0.76	0.23
	D	444	582	0.76	0.24
	TD	446	592	0.75	0.24

slightly larger ferrite grain size evident in Fig. 2.

3. Methods

CVN-mod samples in L-T orientation with the geometry shown in Fig. 3 were machined from the undeformed end-sections of the L-T oriented DWTT samples and centered on the mid-line of the plate thickness as for the CVN samples tested by Mitchell *et al.* [59]. The L-T orientation was selected for the CVN-mod samples to mirror splitting observed in full-scale pipeline burst tests [23]. The sample thickness was 12 mm and 1 mm deep side grooves were introduced by electrical discharge machining (EDM), resulting in a final fracture area (80 mm^2) equivalent to that for a standard CVN sample. The primary V-notch conformed to the standard 2 mm deep ASTM geometry [23]. Fig. 4 presents a photomontage of a single CVN-mod sample to show the side groove geometry as viewed from the bottom, side, and top of the sample. The side-grooves were obtained utilizing the finest EDM wire available, which produced ≈0.2 mm wide grooves with a ≈0.1 mm notch radius.

Test data over the temperature range of −180 °C to 100 °C were obtained on a high-capacity 953 J test machine equipped with an instrumented striker with 8 mm radius of the striking edge. The same machine was utilized without instrumentation for the CVN testing by Mitchell *et al.* [59]. One CVN-mod specimen and sometimes two CVN specimens per temperature were tested, as emphasis

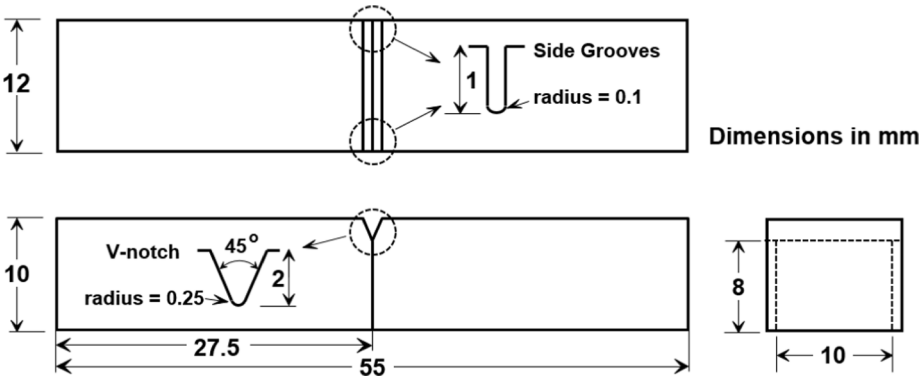

Fig. 3. Geometry of the side-grooved modified Charpy V-notch (CVN-mod) sample, all dimensions in mm [10,11]. Side-groove tolerances: length to edge angle 90° ± 2°, alignment with the V-notch ± 0.025 mm, depth ± 0.025 mm, and root radius ± 0.025 mm.

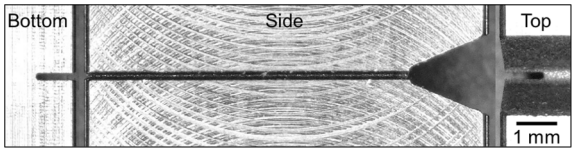

Fig. 4. Photomontage of a CVN-mod sample showing the bottom, side, and top views of the side groove notch introduced by EDM.

was put on representing the material impact behavior through a relatively wide range of testing temperatures.

As the presence of splits may affect calculations based on measurements of lateral expansion and shear fracture percentage [59], quantities of interest can be derived from fitting the absorbed energy (E, as provided by the machine encoder) versus temperature (T) data points using appropriate nonlinear functions [61]. Here, we adopt the most commonly used hyperbolic tangent function [62],

$$E = a + b\tanh\left(\frac{T-c}{d}\right) \tag{1}$$

which is center-symmetric with respect to the point of coordinates (c,a). Parameters a and c thus determine the position of the center of symmetry, and parameters b and d modulate the shape of the curve with b acting along the impact energy axis and d along the temperature axis, as shown using arbitrary values in the example plot in Fig. 5. The parameter c can therefore be used to define the DBTT as the temperature that corresponds to the average between upper and lower shelf energies. Similarly, the sum $a+b$ gives the USE, and $2d$ can be taken as the width, in degrees Celsius, of the transition region.

In its given form, Eq. (1) can yield negative values of absorbed energy at low temperatures. To prevent this, the curve could be forced to a fictitious data point with temperature lower than the lowest testing temperature. In the present study, positive values were instead ensured by imposing a constraint inequality on the values of parameters a and b such that:

$$a - b \geq 0 \tag{2}$$

If the condition in Eq. (2) is met, the fit is equivalent to the unconstrained one obtained using Eq. (1) alone. Otherwise, an optimum fit of positive energy is calculated that would give $E = 0$ at an imaginary $T = -\infty$ and thus $a = b$.

The advanced capability of the Python library for non-linear least square minimization (lmfit) [63,64] was used for fitting the experimental data. This analysis also provided individual standard deviations of the four parameters in Eqs. (1) and (2), which were here used to assess the accuracy of quoted values for USE, DBTT, and width of the transition region. The Python code has been uploaded onto an open science framework (OSF) public repository [65].

3.1. Assessment of splitting in CVN and CVN-mod samples

Several different approaches have been utilized to quantify the extent of splitting observed on fracture surfaces. In early studies of delamination of plate steels, the degree of splitting was estimated by counting the number of splits present on the fracture surface [66]. More recently, the sum of the split lengths has been proposed as a more suitable measure [67]. However, such a measure is insensitive to the lateral dimension (*i.e.* opening) of a split, which can be assumed to be an indicator of its depth. In the present study, the areas of split marks on fracture surfaces were measured to simultaneously account for the split lengths and average split openings.

Grayscale (8-bit) images of the fracture surfaces were acquired at the same spatial resolution and lighting conditions, making sure images were not under- or overexposed. The fracture surfaces were cropped to create new images that were then analyzed separately using the Python scikit-image library for image processing [68], as illustrated in Fig. 6. As for curve fitting, the Python code for the

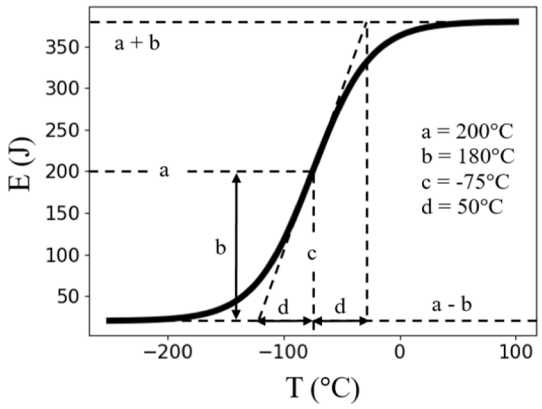

Fig. 5. Geometrical interpretation of the four parameters of the hyperbolic tangent function in Eqs. (1) and (2). The values of the four parameters were arbitrarily chosen for illustrative purposes.

image processing procedure described below has been uploaded onto the public OSF repository [65].

In delaminated samples, the splits appear darker than the surrounding regions so thresholding low pixel intensities of fracture surface images would produce split marks**.** In the image analysis procedure incorporated here, a suitable threshold value was identified as the minimum pixel intensity in a sufficiently large area that were manually selected within the (macroscopically) flat fracture surface of a sample tested at lower shelf energy temperatures, Fig. 6**(a)**. The threshold was then automatically applied to the remaining images, as illustrated in Fig. 6**(b) and 6(c)**. Hence, unwanted features, such as marks left by dark regions between detached halves of broken samples, were manually removed, Fig. 6**(d)**. Automated hole filling and size filtering was then applied to remove the smallest point-like features, Fig. 6**(e)**. The degree of splitting was finally calculated as the splitting ratio S_r, in percentage, between the total area of the identified split marks A_{splits} and the image size A_{total}:

$$S_r = 100 \times \frac{A_{splits}}{A_{total}} \tag{3}$$

4. Results

Evaluation of the CVN-mod testing method and the effects of splitting on impact energies are presented in separate sections. Both the CVN and CVN-mod samples of the three X70 plate steels, as well as the respective datasets, are hereafter referred to as X70-13.5, X70-15.5 and X70-22.

4.1. Comparison between CVN-mod and standard CVN tests

Impact energy as a function of test temperature results for the CVN [60] and CVN-mod samples along with the functional fits for the three steels are shown in Fig. 7**.** The vertical lines and shaded gray areas identify the DBTTs based on the average energy definition in Section 3 and their standard deviations (widths of gray bands), respectively. As evident in the same figure, the CVN-mod data align significantly better to the functional fit than for the corresponding standard CVN sample data for each of the three steels.

Table 4 summarizes the values and standard deviations of the fitting parameters, and the corresponding values of USEs, DBTTs, and temperature ranges associated with the transition from ductile to brittle behavior. The standard deviations for all CVN-mod data are significantly lower than the corresponding values for standard CVN data, demonstrating that the CVN-mod data provided a more accurate evaluation of the impact properties of interest. As shown in Table 4, the USEs for the X70-13.5 and X70-15.5 steels decrease respectively from about 394 and 426 J for the standard CVN samples to about 214 and 232 J for the CVN-mod samples. These values correspond to equivalent USE reductions of about 46% for both the X70-15.5 and X70-13.5 steels, consistent with these two steels having similar tensile properties at room temperature. A smaller USE reduction of about 37% is obtained for the X70-22 steel, although significant standard deviations of about ± 43 J (±18%) of *a* and b calculated for the CVN fit increase the uncertainties in the measurement of such reduction for this steel. CVN-mod testing increases the transition region width (2*d*) by about 26% for X70-13.5 steel and 16% for X70-15.5 steel, and the DBTTs for these steels by 5 °C and 20 °C, respectively.

Figs. 8, 9, and 10 show light optical fractographs of standard CVN and CVN-mod samples for the X70–13.5, X70-15.5, and X70-22 steels, respectively. Also shown below each fractograph is the corresponding identification of the splits by the image analysis procedure described above. The fractured samples exhibited three characteristics during testing: (1) complete separation in two parts; (2) essentially complete fracture with two parts connected by a remaining ligament; and (3) incomplete fracture and extensive plastic deformation. As in previous studies of high-toughness plate steels [4], the latter characteristic was observed for the standard CVN tests at USE temperatures (*i.e.* −40 °C and higher). In contrast, the CVN-mod samples fully broke at the highest testing temperatures,

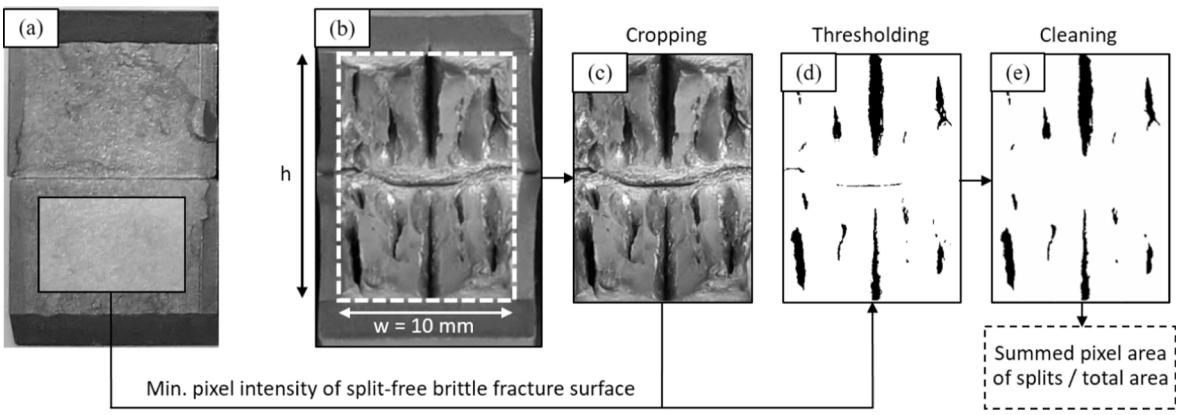

Fig. 6. Main steps in the imaging processing procedure used to assess the degree of splitting in CVN and CVN-mod specimens using CVN-mod X70-13.5 sample tested at −196 and −75 °C as examples. (a) A sufficiently large area of a brittle fracture surface is used to calculate the threshold value, (b) and (c) cropping, (d) application of pixel intensity threshold, (e) manual removal of horizontal features and automated cleaning methods to remove point-like features.

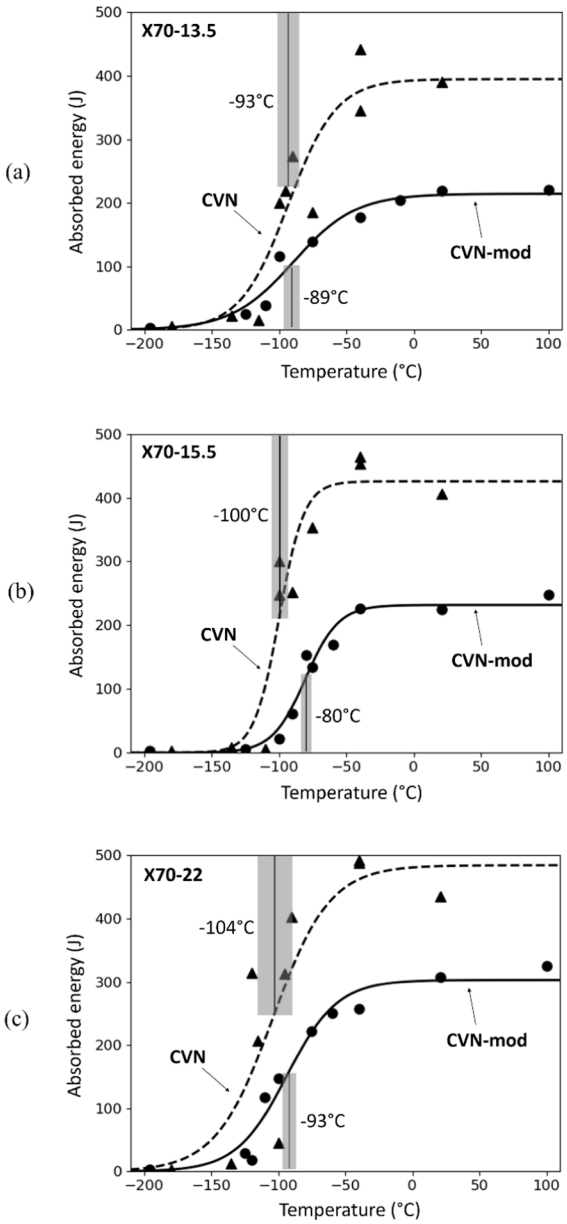

Fig. 7. Absorbed energy *vs.* temperature data points and curve fits obtained for the standard CVN and CVN-mod geometries for the (a) X70-13.5 steel, (b) X70-15.5 steel, and (c) X70-22 samples. Vertical lines and gray areas respectively indicate the value and plus/minus the standard deviation of DBTTs.

Table 4
Fit Parameters and Standard Deviations of the Constrained Hyperbolic Function in Equations (1) and (2) for the Investigated Materials. HTR Stands for one Half of the Transition Region.

Material	Geometry	a ± σ_a (J)	b ± σ_b (J)	c ± σ_c (DBTT, °C)	d ± σ_d (HTR, °C)	a + b (USE, J)
X70-13.5	CVN	197 ± 24	= a	−93 ± 8	36 ± 17	394
	CVN-mod	107 ± 6	"	−89 ± 6	46 ± 12	214
X70-15.5	CVN	213 ± 18	"	−100 ± 4	19 ± 9	426
	CVN-mod	116 ± 6	"	−80 ± 3	24 ± 6	232
X70-22	CVN	242 ± 43	"	−104 ± 13	42 ± 29	484
	CVN-mod	151 ± 9	"	−93 ± 5	38 ± 8	302

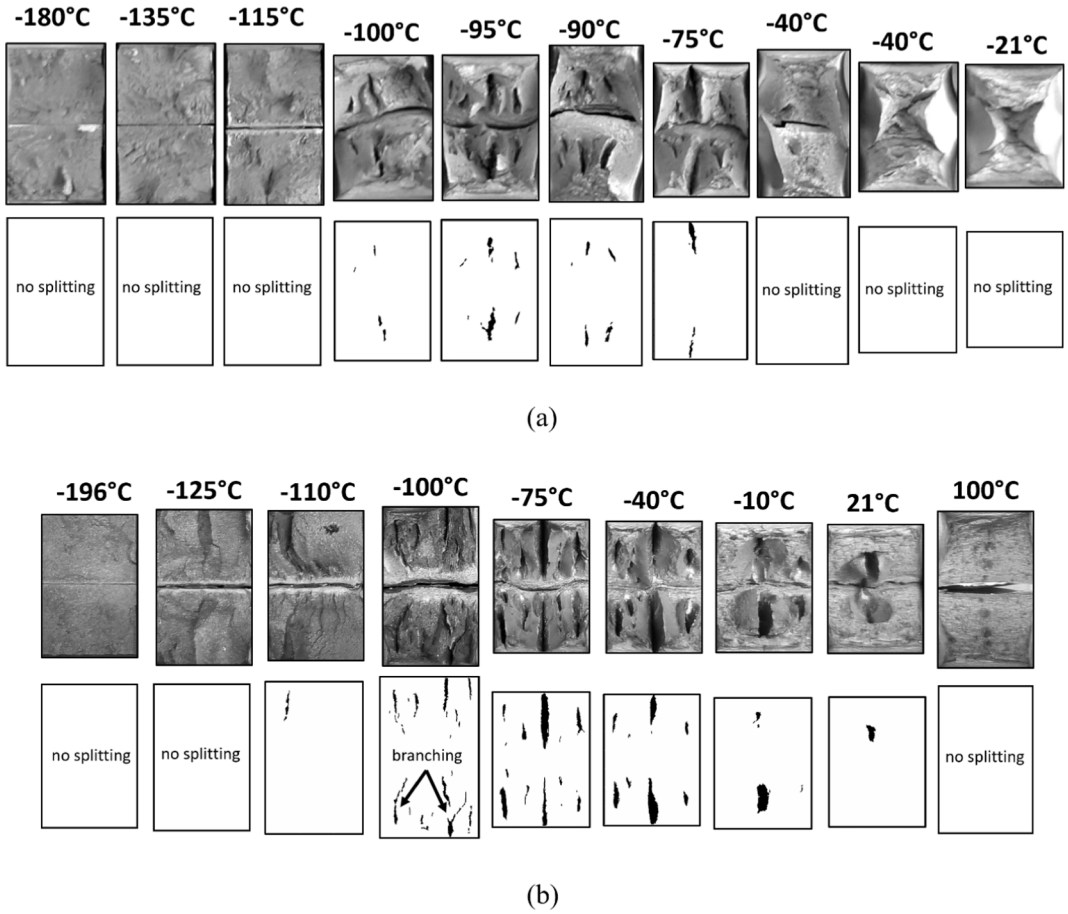

Fig. 8. Light optical fractographs of (a) CVN and (b) CVN-mod specimens of X70-13.5 steel, and outputs of the image processing procedure for split identification. The horizontal dimension of each image equals 10 mm; the notch locations and sample orientations are the same as shown in Fig. 1 **(c);** and for samples which did not completely fracture, the photographed area is smaller and reflects the projected image viewed by the camera.

showing reduced lateral expansion that is indicative of higher stress triaxiality. For both geometries, some samples which exhibited splitting at intermediate temperatures exited the anvil with the final ligament intact (*i.e.* characteristic (2)). The light optical fractographs for these samples are thus projections of the fracture surfaces on the plane of view and appear in Figs. 8, 9 and 10 as images slightly smaller than those obtained for samples which completely failed at the lower temperatures. However, evaluation of the ratio S_r was not affected, as both area terms (*i.e.* A_{splits} and A_{total}) in Eq. (3) were reduced by the same fraction.

Splitting is detected in all three materials in the transition temperature range. For the X70-22 steel, in particular, splitting is not detected in the CVN fracture surfaces but found in the CVN-mod fracture surfaces of samples tested between −100 and −75 °C. Splitting over a wider range of temperatures, including room temperature, is observed for the CVN-mod fracture surfaces of the X70-15.5 and X70–13.5 steels.

Fig. 8 shows that large central splits occurred in the X70–13.5 steel for both the CVN and CVN-mod samples. The occurrence of these splits was attributed to the presence of a distinct pearlite band at the plate centerline [59]. These central splits in the CVN-mod samples tested at −75 and −40 °C are present at the notch root, suggesting that splits initiate prior to the propagation of the main crack. In contrast, the splits in the CVN-mod fracture surfaces for X70-15.5 steel (Fig. 9) appear more evenly distributed, even when compared with the CVN fracture surfaces for the same material.

Values of splitting ratio, S_r, in Eq. 3 are plotted as a function of temperature in Fig. 11**(a), 11(b), and 11(c)** for the X70-13.5, X70-15.5, and X70–22 steels, respectively. The dashed (CVN) and solid (CVN-mod) lines represent linearly interpolated values. For each steel, the variation of the degree of splitting with temperature approximates a right-skewed bell-shaped curve with the maxima at temperatures close to the DBTTs (values for both CVN and CVN-mod data are also indicated in the figures). For the X70-15.5 steel, a spike in the degree of splitting is observed at −80 °C, which can be associated with the branching of the splits highlighted using black arrows in Fig. 9**.** Split branching was also observed for the X70–13.5 sample tested at −100 °C, as shown in Fig. 8. In the X70–13.5 steel, however, branching was accompanied by the loss of the most prominent central splits so that the overall severity of splitting decreased.

The quantified splitting measurements for the three steels were directly compared on a single plot in Fig. 12**(a)**, which shows that splitting is most intense in the X70-13.5 steel at all temperatures for which delamination is observed. The degree of splitting is instead

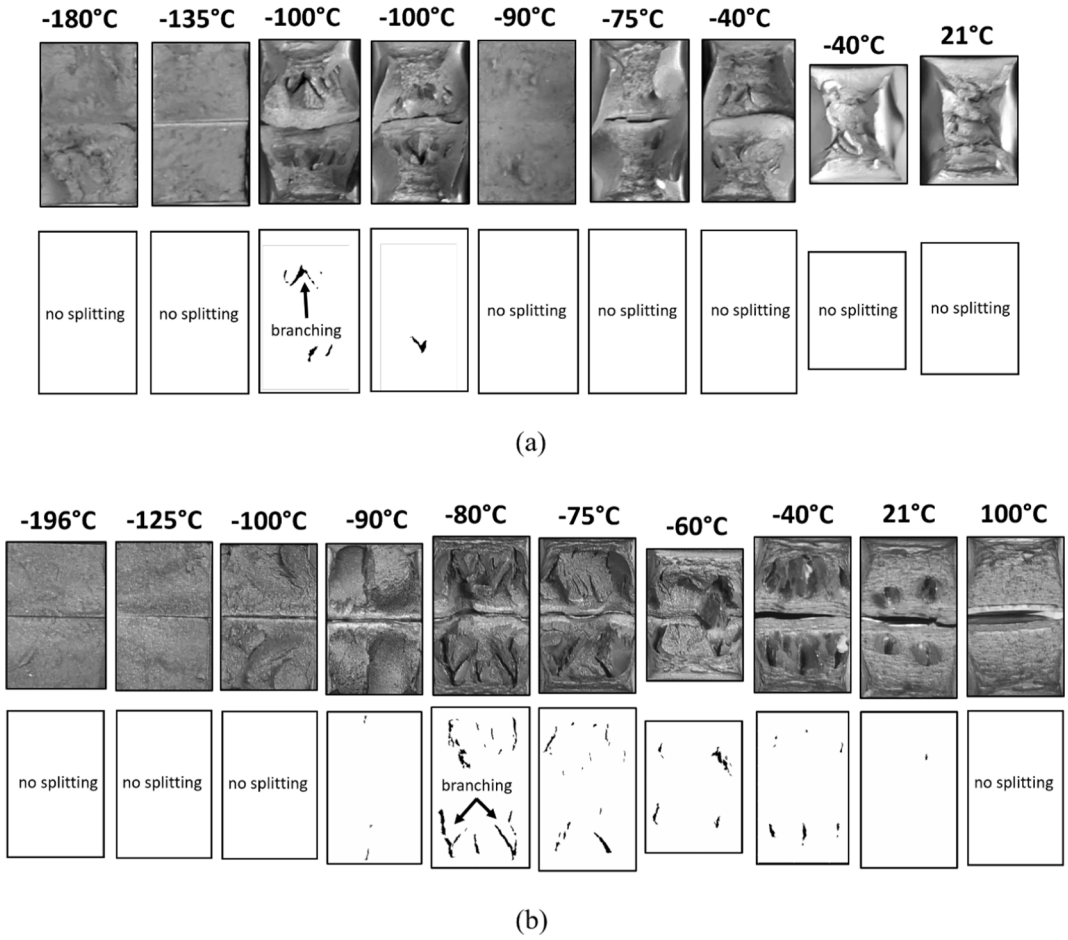

Fig. 9. Light optical images of fractured (a) CVN and (b) CVN-mod specimens of X70-15.5 steel, and outputs of the image processing procedure for split identification. The horizontal dimension of each image equals 10 mm; the notch locations and sample orientations are the same as shown in Fig. 1**(c).** For samples which did not completely fracture, the photographed area is smaller and reflects the projected image viewed by the camera.

similar for X70-15.5 steel and X70-22 steel, although distributed differently among testing temperatures as described above.

4.2. Comparison between relative splitting susceptibilities in CVN-mod test and DWTT

In Mitchell *et al.* [59], standard pressed notch DWTT specimens were machined in accordance with API RP-5L3 [27] from the three steel plates investigated here. DWTT temperatures were chosen iteratively by first establishing upper and lower shelf temperatures, and by then choosing two transitional test temperatures to characterize the transition region. DBTTs were calculated as the temperature corresponding to 85% shear area ($DBTT_{85}$), and the degree of splitting was based on a "separation index" measure defined as the ratio between the sum of the length of all splits and the inspected area.

The distinct nature of DWTT and the still unclear effects of abnormal fracture on DWTT results of high–toughness steels, which have been described above and observed for the three steels in Mitchell *et al.* [59], limit direct comparisons with the CVN-mod results presented here. However, agreement may be expected between the differences in splitting severity obtained by the two testing methods, as the CVN-mod test is designed to mimic the highly constrained conditions of full-thickness DWTT samples.

Data for areas in the central portions of the plates on DWTT samples machined in the L-T orientation were selected for analysis and replotted as separation index versus test temperature in Fig. 12**(b)**. The results based on the DWTT samples were obtained for temperatures below −20 °C and exhibit many of the same characteristics shown by the data for the CVN-mod results shown in Fig. 12**(a)** for corresponding test temperatures. Specifically, the splitting susceptibility for the X70-13.5 is highest at any testing temperature, independent of test technique. Furthermore, both figures show that at low temperatures the splitting susceptibility of the X70-22 steel is slightly greater than for the X70-15.5 steel. Even though the temperature ranges differ slightly between Fig. 12**(a) and 12(b)**, the comparison between the two figures suggests that CVN-mod data provide the similar assessment of relative splitting susceptibilities between steels as observed for DWTT data.

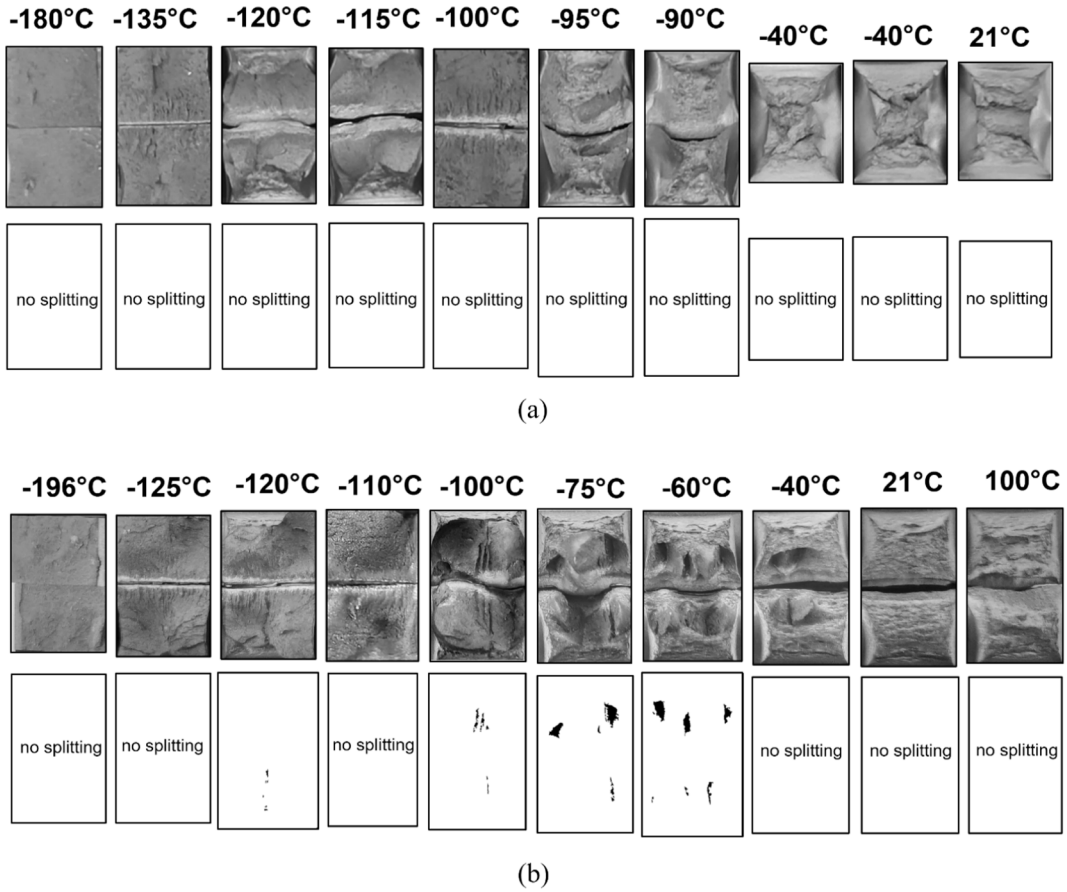

Fig. 10. Light optical images of fractured (a) CVN and (b) CVN-mod specimens of X70-22 steel, and outputs of the image processing procedure for split identification. The horizontal dimension of each image equals 10 mm; the notch locations and sample orientations are the same as shown in Fig. 1**(c)**; and for samples which did not completely fracture, the photographed area is smaller and reflects the projected image viewed by the camera.

4.3. Comparison between CVN-mod tests of X70 Ferrite/Pearlite steels

CVN-mod impact energies as a function of temperature for the X70-15.5 and X70-13.5 steels in Fig. 7**(a) and 7(b)** are replotted together in Fig. 13**(a).** In comparison to the impact toughness for the X70–15.5 steel, measured energies for the X70-13.5 steel are lower above −76 °C and higher below this temperature. An additional point highlighted in Fig. 13**(a)** by the data encircled by the dashed line and identified as exhibiting split branching is that the only data points above the hyperbolic tangent curves are those belonging to samples that show split branching.

To facilitate characterization of the effect of splitting on impact energies, the difference between CVN-mod energy values of the curve fits for X70-13.5 and X70-15.5 steels were calculated and correlated with the difference between the piecewise linear curves of the corresponding splitting ratio (S_r) in Fig. 12**(a)**, following the removal of the two data points affected by split branching. The results are plotted in Fig. 13**(b)** using solid and dashed lines, respectively. A maximum negative difference in impact energy (-38 J) is obtained between −76 °C and USE temperatures, and a maximum positive difference (42 J) is reached below –76 °C. Splitting is thus found to increase energy absorption at low temperatures and decrease the corresponding values by a similar extent at higher temperatures. The difference in energies is therefore minimum close to the DBTTs despite the corresponding difference in splitting being highest at such temperatures. The primary effect of splitting on impact energies is thus to expand the temperature range associated with the ductile-to-brittle transition, consistent numerically with the fitting parameter d of the X70-13.5 steel being higher than the one calculated for X70-15.5 steel (see bold values in Table 4).

5. Discussion

In the present study, CVN-mod test data exhibit significantly reduced deviation from the hyperbolic tangent fit as compared to standard CVN data. The reduced scatter observed for all three steels can be attributed to the side grooves limiting the high variability of impact energy that may be associated with stochastic topology of shear lips [69]. The ability of the CVN–mod test to improve the

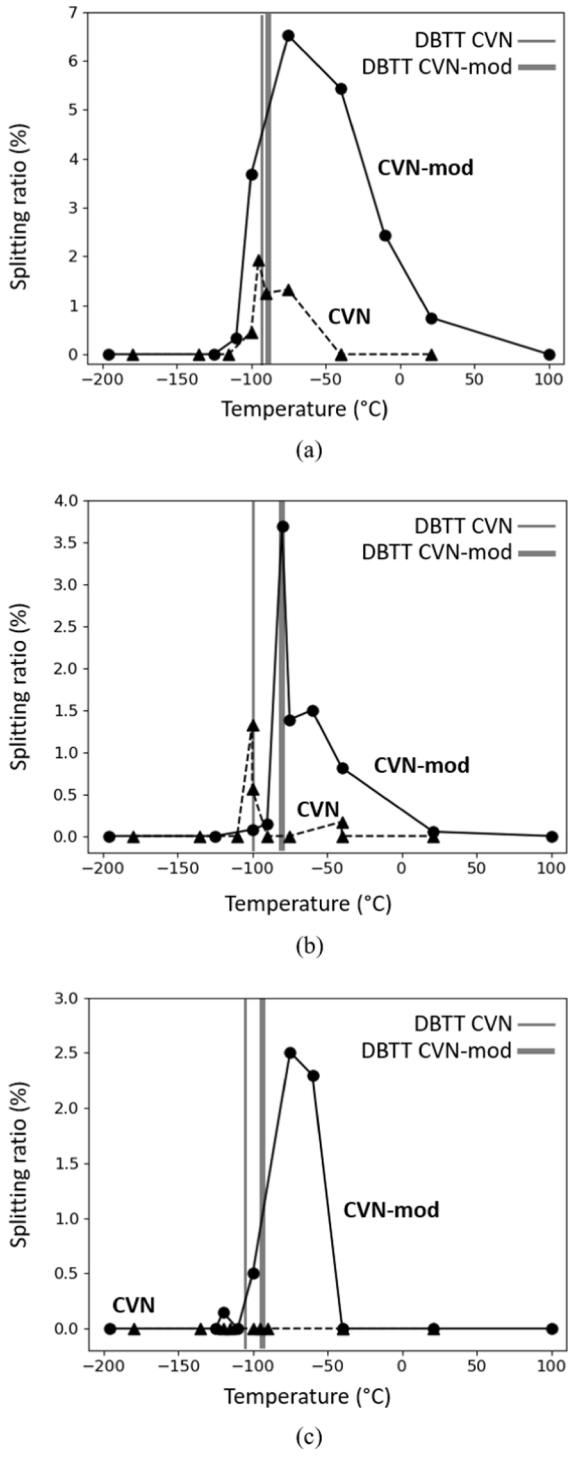

Fig. 11. Effect of test temperature on the degree of splitting calculated as percentage of area of the split marks over each fracture surface from the splitting maps shown in Figs. 8, 9 and 10: (a) X70-13.5 steel, (b) X70-15.5 steel, and (c) X70-22 steel.

accuracy of impact property measurements has a practical advantage to reduce the number of impact tests required to compare performance between plate steels. Moreover, the CVN-mod geometry increases stress triaxiality conditions akin to those experienced by the central section of full-thickness plates, consistent with the CVN-mod tests here yielding differences in splitting susceptibilities between the investigated materials that agree qualitatively with the differences observed in previous DWTT tests [59].

By modulating through-thickness stress triaxiality, the depth and width of the side-grooves have been shown elsewhere to affect

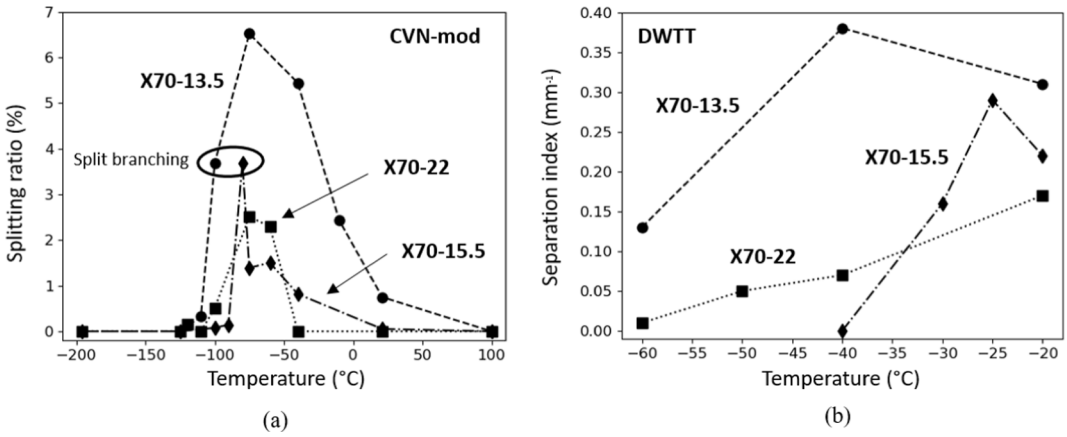

Fig. 12. (a) Temperature dependence of the degree of splitting for the CVN-mod tested X70–13.5, X70-15.5, and X70-22 steels. (b) Temperature dependence of the "separation index" used in Mitchell *et al.* [59] for the DWTT samples machined in L-T orientation.

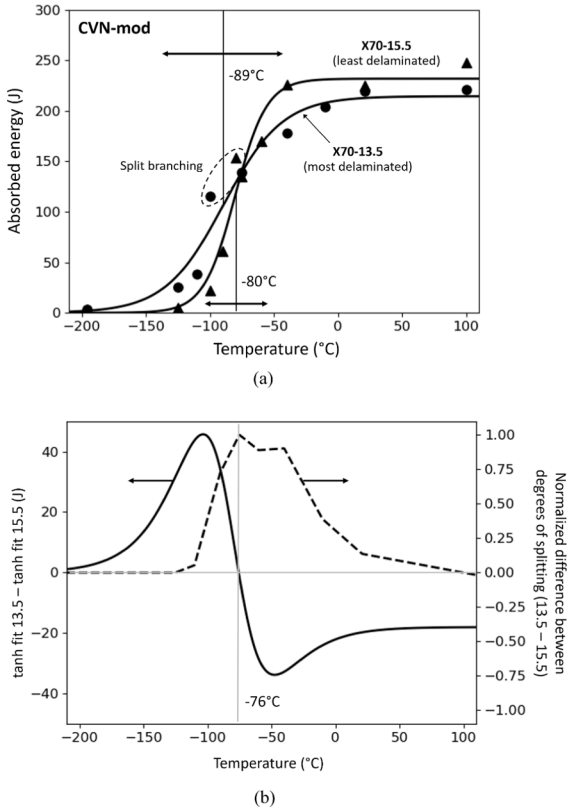

Fig. 13. (a) Absorbed energy *vs.* temperature data points and curve fits for the CVN-mod tests of the X70–13.5 and X70-15.5 samples in Fig. 7**(a) and 7(b)**. Vertical lines indicate DBTTs, whereas horizontal arrows highlight the size of the transition region given as 2*d*; and (b) the difference between fitted tanh curves of X70-13.5 and X70-15.5 tests compared with the corresponding difference between interpolated splitting degrees in Fig. 12**(a)** (data for samples which exhibited split branching were excluded).

crack initiation location along the notch root and the shape of the crack front [5]. Increasing the acuity of side grooves beyond a critical value would eventually result in crack initiation at the intersection of the V-notch and the side grooves [5]. Therefore, material-dependent side-grooved geometries [21,70] for the CVN-mod testing of high-toughness steels may exist that are optimized to induce near-uniform crack initiation and significant stress triaxiality below the V-notch. This specific modification of side-groove geometry will be subject of future work using finite element analysis.

In addition to reducing scatter, the CVN-mod geometry has been shown to promote splitting and split branching. This observation

confirms that the additional constraint due to the presence of the side-grooves enhances the magnitude of the induced tensile stresses perpendicular to fracture sensitive microstructural regions in L-T samples machined from hot-rolled plates.

Consistent with results from previous studies [32,71,72], the presence of a pearlite-rich centerline in plate steels has been found to promote splitting, as demonstrated by the formation of a prominent central split in the fracture surfaces of the X70-13.5 CVN and CVN-mod samples. The central split nevertheless disappeared at the lowest testing temperature within the transition region to be replaced by smaller but more numerous splits with branching features that resemble the macroscopic branching of cracks in brittle materials. This phenomenon suggests that the formation of the severe central split in the X70-13.5 steel, and therefore the cause of the relatively high splitting susceptibility of its pearlite-rich microstructure, are associated with damage due to plastic strain accumulation and incompatibility between microstructural components [73], such as that imagined to arise between clusters of cube-oriented grains in Ghosh *et al.* [38]. Similarly, the ferrite/bainite X70-22 steel appeared less susceptible to splitting than the ferrite/pearlite X70-13.5 and X70–15.5 steels possibly because of more uniform plastic strains at the microstructural length scale. Mapping of plastic deformation at grain-scale [74] and submicron spatial resolutions [75–77] would be however required to provide experimental evidence of plastic incompatibility leading to splitting.

The comparison shown in Fig. 13 between steels of similar tensile properties but different splitting susceptibilities exposed a dual, temperate-dependent effect of splitting on impact energies that is least intense at temperatures close to the DBTT where splitting severity is greatest. The origins of this effect can be found in force–displacement data obtained in instrumented impact tests. With the cross-over temperature of −76 °C in Fig. 13**(b)** as a reference, Fig. 14**(a)** compares force–displacement data for the two steels at a temperature (–100 °C) below the cross-over temperature, and Fig. 14**(b)** compares data at –40 °C, a temperature above the cross-over.

As shown in the fractographs in Figs. 8 and 9**,** at –100 °C, splitting was extensive in the X70-13.5 steel and almost absent in the X70-15.5 steel, and Fig. 14**(a)** reflects these differences. The force–displacement curve for the X70-15.5 steel shows an abrupt force drop associated with the onset of unstable crack growth [78], a behavior characteristic of brittle fracture at low temperatures. In contrast, the continuous force–displacement curve for the X70-13.5 sample is characteristic of plastic deformation associated with ductile fracture, a consequence of splitting which relaxes the local (tensile) stresses and promotes localized plasticity. Thus, splitting increases the absorbed energy at low temperatures. At temperatures above the cross-over temperature where plasticity dominates fracture in both materials, the data obtained at −40 °C in Fig. 14**(b)** show that there is less resistance to crack growth (*i.e.* lower force–displacement curve) in the X70-13.5 sample which exhibited extensive splitting. Thus, splitting decreases the absorbed energy at high temperatures.

At a particular temperature in the range of transitional temperatures, the dual effect of splitting on impact energies must cancel out. Fig. 15 shows the force–displacement curves obtained for the two steels at −75 °C, which is the testing temperature closest to the cross-over temperature of −76 °C. At point A, both samples achieve similar maximum force. However, as observed in the fractograph for the X70-13.5 steel, splitting initiates close to the notch root with a large central split and extensive secondary splits form with crack growth. As a consequence of this splitting behavior, the forces required to maintain stable ductile fracture decrease to produce the observed continuous decrease in the force–displacement curve. In contrast, for the X70-15.5 steel, which exhibits limited splitting, initial growth of a ductile crack spanning the sample width requires higher forces with a gradual force decrease. The gradual force decrease continues to point B, at which an abrupt force drop of 12 kN to point C is recorded, associated with an increment of rapid unstable crack growth. Stable crack growth is recovered at point C where the rate of force decrease for the two steels match. At point D, a second, smaller, force drop of 3 kN to point E is observed for the X70-15.5 test. For the X70-13.5 steel, energy absorption continues to gradually decrease past point D so that relevant energy absorption continues until full fracture at point F. As similar areas are delimited between the points ABC and points DEF, the two samples exhibit essentially the same total absorbed energies.

In contrast to CVN observations, CVN-mod testing has shown that X70-22 steel with a ferrite/bainite microstructure is susceptible to splitting, although generally less so than the ferrite/pearlite steels. Having different mechanical properties, the absorbed energy for the X70-22 steel has not been included in the comparison between CVN-mod data in Section 4.3**,** which was aimed at isolating the effects of splitting on impact energies in two steels with similar mechanical properties. However, a striking similarity has been found between the force–displacement curve obtained for the X70-22 steel at −100 °C and the one obtained for the X70-15.5 steel at −75 °C, as shown in Fig. 16**.** This correspondence suggests that yield and ultimate tensile strengths for the X70–22 steel at room-temperature may have increased with decreasing temperature to equal those of the X70-15.5 steel at −75 °C. This aspect alone, however, would not explain the matching shape of the two curves. Interestingly, –100 °C is close to the DBTT of −95 °C for the X70-22 steel and the temperature at which the degree of splitting of the X70–22 steel reached a maximum as in Fig. 12**(a)**. Furthermore, the degree of splitting at such a temperature is similar to that calculated for the X70-15.5 steel at −75 °C, as shown in the same figure. The coincidental occurrence of the two materials having similar tensile properties as well as splitting susceptibilities at these temperatures may thus explain the similarities of impact responses.

The dual effect of splitting on impact energies described above has been found to primarily expand the temperature range associated with transition from ductile to brittle behavior, towards both lower and higher temperatures. The increase in the transition temperature range reflects both the detrimental effect of lowering crack arrestability at high temperatures and the beneficial effect of providing a gentler ductile-to-brittle transition at lower temperatures. This observation suggests that the performance of plate steels in pipeline applications may be improved by reducing splitting susceptibility, if these steels show poor crack arrestability at service temperatures, or by increasing splitting susceptibility, if these show an abrupt ductile–to–brittle transition so that enhanced low temperature toughness is required.

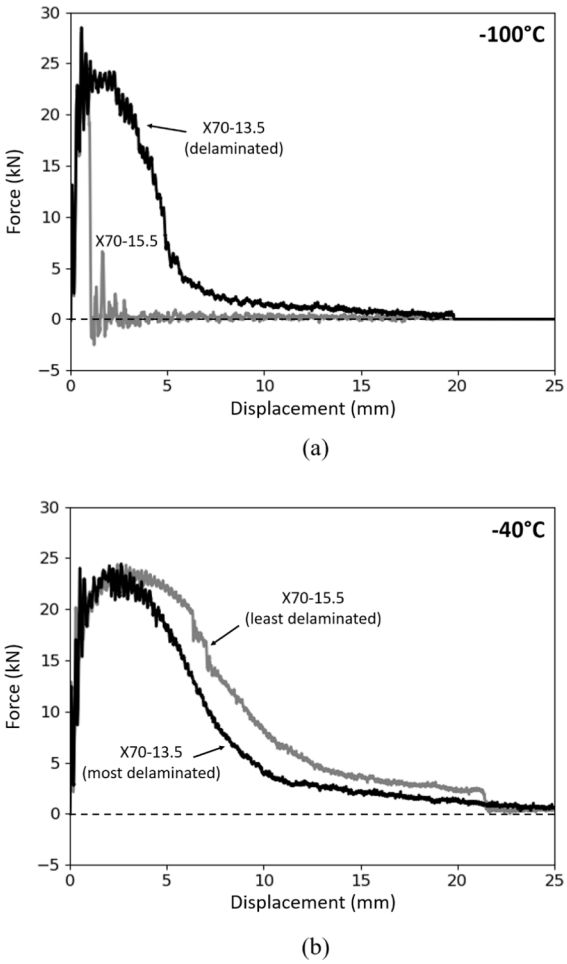

Fig. 14. Force-displacement curves from instrumented CVN-mod tests on X70-15.5 and X70-13.5 steels at the transitional temperatures of (a) −100 °C (*i.e.* below the DBTTs of both materials), and (b) −40 °C (*i.e.* above the DBTTs of both materials).

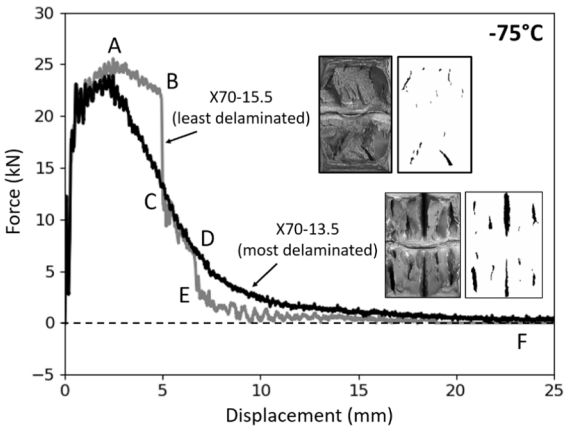

Fig. 15. Force-displacement curves from instrumented CVN-mod tests on X70-15.5 and X70-13.5 steels at the transitional temperature of −75 °C (*i.e.* close to the DBTTs of both materials and to the temperature of −76 °C at which the interpolated values of the absorbed energies in Fig. 11 **(b)** coincide).

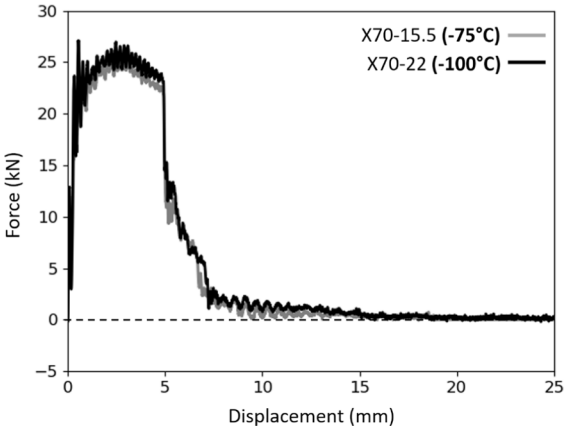

Fig. 16. Force-displacement curves from instrumented CVN-mod tests on X70-15.5 steel at −75 °C (*i.e.* close to its DBTTs of −80 °C) and of the X70-22 steel at −100 °C (*i.e.* close to its DBTT of –93 °C).

6. Conclusions

A modified Charpy impact test (CVN-mod) which incorporate side grooves has been evaluated by comparison with the standard CVN test. Two high-toughness X70 plate steels with a ferrite/pearlite microstructure and a third that exhibits a ferrite/bainite microstructure have been investigated. Fitting of the data points with a constrained hyperbolic tangent function has been used to quantify changes and measurement accuracy of USEs, DBTTs, and width of the transition regions. Consistent with the observations of other side-grooved geometries, the CVN-mod test lowers the values of USE below the maximum capacity of conventional Charpy equipment (300 J – 450 J), making testing of the new high-toughness plate steels available at more laboratories. Moreover, the CVN–mod test decreases the variability of Charpy measurements, reducing the number of impact tests required to assess fracture properties with sufficient accuracy. Although the CVN-mod geometry is not currently covered in ISO 148–1 [22] or ASTM E23 [23], alternative specimen configurations are allowed in both test standards (Annex A3 and Table 2, respectively). The standard test procedure is generally applicable to CVN-mod specimens, without the need for significant modifications or adjustments.

The presence of side grooves has been shown to promote splitting, which has been quantified using a novel image analysis procedure that accounts for both the total split lengths as well as the degree of split opening on the fracture surface. Consistent with the enhancement of stress triaxiality, the differences in splitting susceptibilities between the investigated materials agree qualitatively with those observed in previous DWTT of full–thickness samples.

The direct comparison between two ferrite/pearlite steels that differed only with respect to the splitting susceptibility has made it possible to isolate the effect of splitting on Charpy impact energies, which was also reflected in force–displacement curves at representative temperatures. Splitting has been found to counteract unstable fracture at low temperatures and reduce crack growth resistance at high temperatures. As the effects of these actions on impact energies were seen to cancel out at a transitional temperature close to the DBTT, it has been shown that the primary consequence of splitting on impact properties is to extend the ductile-to-brittle transition about such intermediate temperature.

Declaration of Competing Interest

The authors declare that they have no known competing financial interests or personal relationships that could have appeared to influence the work reported in this paper.

Acknowledgements

The authors acknowledge support of the corporate sponsors of the Advanced Steel Processing and Products Research Center at the Colorado School of Mines. The authors also thank the staff of the National Institute of Standards and Technology in Boulder, Colorado for access to the instrumented high-capacity impact test system utilized for CVN-mod and CVN testing. Saudi Basic Industries Corporation (SABIC) and Baosteel Group are acknowledged for providing the plate material material.

Data Availability

The raw data required to reproduce these findings are available to download from https://osf.io/ekv6j/. The processed data required to reproduce these findings cannot be shared at this time due to technical or time limitations.

References

[1] Boulger FW. Fracture Toughness Comparisons in Steels. Fract. Met., Elsevier 1969:181–246. https://doi.org/10.1016/b978-0-12-449706-1.50009-3.
[2] Recommended Practice for Conducting Drop-Weight Tear Tests on Line Pipe, API RP 5L3, American Petroleum Institute, Washington DC, 1996.
[3] Yang Z, Kim CB, Feng Y, Cho C. Abnormal Fracture Appearance in Drop-weight Tear Test Specimens of Pipeline Steel. Mater. Sci. Eng. A. 2008;483–484:239–41. https://doi.org/10.1016/j.msea.2006.09.182.
[4] M. Manahan, Constraint-Modified, Charpy-Sized Fracture Toughness Specimen for Pipeline Testing, in: AISTech 2013 -The Iron Steel Technol. Conf. Expo., Pittsburgh, PA, 2013.
[5] Birkbeck G, Wraith AE. Influence of Crack Shape on Crack Opening Displacement Measurements Using Charpy Specimens. Metall. Mater. Trans. 1970;1:1474–6. https://doi.org/10.1007/BF02900285.
[6] Zhang XP, Shi YW. Fracture toughness of Charpy-size compound specimens and its application in engineering. Int. J. Press. Vessel. Pip. 1994;57:91–8. https://doi.org/10.1016/0308-0161(94)90102-3.
[7] E. Lucon, European Activity on Instrumented Impact Testing of Subsize Charpy V-notch Specimens (ESIS TC5), in: ASTM Spec. Tech. Publ., ASTM International, 2000: pp. 242–252. Doi: 10.1520/stp14398s.
[8] Emrich A, Mühlich UM, Kuna M, Ludwig A, Trubitz P. Indirect Measuring of Crack Growth by Means of a Key-curve-method in Pre-cracked Charpy Specimens Made of Nodular Cast Iron. Int. J. Fract. 2007;145:47–61. https://doi.org/10.1007/s10704-007-9105-2.
[9] Kondryakov EA, Panasenko AV, Kharchenko VV. Experimental Determination of the Moment of Fracture Initiation in Standard Charpy Specimens and Specimens with Edge Notches. Strength Mater. 2015;47:291–6. https://doi.org/10.1007/s11223-015-9658-7.
[10] Al-Jabr HM. Influence of Crystallographic Texture in X70 Pipeline Steels on Toughness Anysotropy and Delamination. Golden, CO USA: Colorado School of Mines; 2017.
[11] H.M. Al-Jabr, D.K. Matlock, J.G. Speer, Modified Impact Testing Method to Evaluate Toughness of Higher API Grades, in: R. Bodnar, A. De, T. Ros-Yanez, J.G. Speer, Q. Yu (Eds.), 2nd Int. Symp. Recent Dev. Plate Steels, AIST, Warrendale, PA, 2018: pp. 253–261.
[12] Lucon E. Cost-Effective Alternatives to Conventional Charpy Tests for Measuring the Impact Toughness of Very-High-Toughness Steels. J. Press. Vessel Technol. Trans. ASME. 2018;140. https://doi.org/10.1115/1.4038902.
[13] E. Kondryakov, O. Panasenko, A. Kravchyk, V. Kharchenko, Peculiarities of the Crack Initiation and Propagation in Different Specimen Types, in: Procedia Struct. Integr., Elsevier B.V., 2019: pp. 43–50. Doi: 10.1016/j.prostr.2019.07.020.
[14] Smith E, Patchett BM. Effects of Notch Acuity and Side Grooving on Fracture Toughness. Part I-Impact Loading. Weld. Res. Suppl. 1975:169–77.
[15] E. Smith, B.M. Patchett, Effects of Notch Acuity and Side Grooving on Fracture Toughness. Part II -Slow Bend, Weld Res. Suppl. (1975) 226–234.
[16] Nguyen-Duy P, Phelippeau G, Simoneau R, Begin G. The Determination of the J-integral on Precracked Charpy Specimens by Instrumented Impact Testing and Slow-bend Testing. J. Eng. Mater. Technol. Trans. ASME. 1978;100:253–7. https://doi.org/10.1115/1.3443487.
[17] Server WL, Wullaert RA, Ritchie RO. On the Use of Side-grooves in Estimating JIC Fracture Toughness with Charpy-size Specimens. J. Eng. Mater. Technol. Trans. ASME. 1980;102:192–9. https://doi.org/10.1115/1.3224796.
[18] Nguyen-Duy P, Bayard S. Brittle-ductile Transition Curve Determined by Charpy Impact Testing on CVN, Precracked CVN and Side-grooved Precracked CVN Specimens. Int. J. Fract. 1982;18:R23–9. https://doi.org/10.1007/BF00019643.
[19] Manahan MP. Determination of Fracture Behavior of Ferritic Steels Using Miniaturized Specimens. J. Nucl. Mater. 1989;166:321–30.
[20] Manahan MP, Charles C. A Generalized Methodology for Obtaining Quantitative Charpy Data from Test Specimens of Nonstandard Dimensions. Nucl. Technol. 1990;90:245–58. https://doi.org/10.13182/NT90-A34418.
[21] Zhang XP, Shi YW. Constraint of Side-groove and its Influence on Fracture Toughness Parameter in Charpy-size Specimens. Eng. Fract. Mech. 1992;43:863–7. https://doi.org/10.1016/0013-7944(92)90016-8.
[22] ISO - ISO 148-1:2016 - Metallic Materials — Charpy Pendulum Impact Test — Part 1: Test Method, (2016). https://www.iso.org/standard/63802.html (accessed April 14, 2021).
[23] ASTM International, ASTM E23 − 18, Standard Test Methods for Notched Bar Impact Testing of Metallic Materials, ASTM Int. (2018) 1–26. Doi: 10.1520/E0023-18.
[24] Tanguy B, Luu TT, Perrin G, Pineau A, Besson J. Plastic and Damage Behaviour of a High Strength X100 Pipeline Steel: Experiments and Modelling. Int. J. Press. Vessel. Pip. 2008;85:322–35. https://doi.org/10.1016/j.ijpvp.2007.11.001.
[25] Pyshmintsev IY, Gervasyev AM, Struin AO, Arabey AB, Yesiev TS. X80 Pipelines in Arctic Environment: Prediction of the Long-distance Ductile Fracture Propagation/arrest, 8th Pipeline Technol. Conf. 2013;2013.
[26] Ruggieri C, Hippert E. Delamination Effects on Fracture Behavior of a Pipeline Steel: A Numerical Investigation of 3-D Crack Front Fields and Constraint. Int. J. Press. Vessel. Pip. 2015;128:18–35. https://doi.org/10.1016/j.ijpvp.2015.01.004.
[27] API 5L Specification for Line Pipe, 46th ed., American Petroleum Institute, Washington DC, 2018.
[28] Mintz B, Morrison WB. Influence of Warm Working and Tempering on Fissure Formation. Mater. Sci. Technol. 1988;4:719–31. https://doi.org/10.1179/mst.1988.4.8.719.
[29] Baldi G, Buzzichelli G. Critical stress for delamination fracture in HSLA steels. Met. Sci. 1978;12:459–72. https://doi.org/10.1179/030634578790433332.
[30] Mintz B. Influence of Grain Boundaries on Fissure Formation During Impact Testing of Ferritic Stainless Steels. Met. Technol. 1980;7:127–9. https://doi.org/10.1179/030716980803287233.
[31] Punch R, Strangwood M, Davis C. Origin and Propagation of Splits in High-strength Low-alloy Strip Steel. Metall. Mater. Trans. A Phys. Metall. Mater. Sci. 2012;43:4622–32. https://doi.org/10.1007/s11661-012-1307-1.
[32] Shanmugam P, Pathak SD. Some Studies on the Impact Behavior of Banded Microalloyed Steel. Eng. Fract. Mech. 1996;53:991–1005. https://doi.org/10.1016/0013-7944(95)00159-X.
[33] Bourell DL. Cleavage Delamination in Impact Tested Warm-rolled Steel. Metall. Trans. A. 1983;14:2487–96. https://doi.org/10.1007/BF02668890.
[34] T. Hara, Y. Shinohara, H. Asahi, Y. Terada, Effects of Microstructure and Texture on DWTT Properties for High Strength Line Pipe Steels, in: Int. Pipeline Conf. 2006, Calgary, CAN, 2006. http://www.asme.org/about-asme/terms-of-use.
[35] Pyshmintsev I, Gervasyev A, Petrov RH, Carretero Olalla V, Kestens LAI. Crystallographic Texture as a Factor Enabling Ductile Fracture Arrest in High Strength Pipeline Steel. Mater. Sci. Forum. 2011;702–703:770–3. https://doi.org/10.4028/www.scientific.net/MSF.702-703.770.
[36] Al Jabr HM, Speer JG, Matlock DK, Zhang P, Cho SH. Anisotropy of Mechanical Properties of API-X70 spiral Welded Pipe Steels. Mater. Sci. Forum. 2013;753:538–41. https://doi.org/10.4028/www.scientific.net/MSF.753.538.
[37] Gervasyev A, Pyshmintsev I, Petrov R, Huo C, Barbaro F. Splitting Susceptibility in Modern X80 Pipeline Steels. Mater. Sci. Eng. A. 2020;772. https://doi.org/10.1016/j.msea.2019.138746.
[38] Ghosh A, Patra S, Chatterjee A, Chakrabarti D. Effect of Local Crystallographic Texture on the Fissure Formation During Charpy Impact Testing of Low-Carbon Steel. Metall. Mater. Trans. A Phys. Metall. Mater. Sci. 2016;47:2755–72. https://doi.org/10.1007/s11661-016-3458-y.
[39] B. Mintz, W.B. Morrison, Influence of Fissures on Tensile and Fracture Toughness of Steels with Ferrite/pearlite Microstructures, 2007. Doi: 10.1179/174328407X168801.
[40] Mintz B, Maina EM, Morrison WB. Influence of Dislocation Hardening, Precipitation Hardening, Grain Elongation and Sulphides on Fissure Formation in HSLA Steels Having a Ferrite/pearlite Microstructure. Mater. Sci. Technol. 2008;24:177–88. https://doi.org/10.1179/174367507X247377.
[41] Farber VM, Khotinov VA, Belikov SV, Selivanova OV, Lezhnin NV, Morozova AN, et al. Separations in Steels Subjected to Controlled Rolling, Followed by Accelerated Cooling. Phys. Met. Metallogr. 2016;117:407–21. https://doi.org/10.1134/S0031918X16040050.
[42] ASTM Standard E1823-20b Standard Terminology Relating to Fatigue and Fracture Testing, ASTM International, West Conshohocken, PA, 2020.
[43] Embury J, Petch N, Wraith A, Wright E. The Fracture of Mild Steel Laminates. Am. Inst. Mining, Metall. Pet. Eng. 1968.

[44] Lesuer DR, Syn CK, Sherby OD, Wadsworth J, Lewandowski JJ, Hunt WH. A Simple Way to Make Tough Ceramics. Int. Mater. Rev. 2012;41:169–97. https://doi.org/10.1179/095066096790151204.
[45] Clegg WJ, Kendall K, Alford NMN, Button TW, Birchall JD. A Simple Way to Make Tough Ceramics. Nature 1990;347:455–7. https://doi.org/10.1038/347455a0.
[46] D.T. Adams, B.L.; Gardner, C.J.; Fullwood, EBSD-based Dislocation Microscopy, Diffus. Defect Data Part B (Solid State Phenomena). 160 (2010) 3–10. Doi: DOI 10.4028/www.scientific.net/SSP.160.3.
[47] Inoue T, Yin F, Kimura Y, Tsuzaki K, Ochiai S. Delamination Effect on Impact Properties of Ultrafine-grained Low-carbon Steel Processed by Warm Caliber Rolling. Metall. Mater. Trans. A Phys. Metall. Mater. Sci. 2010;41:341–55. https://doi.org/10.1007/s11661-009-0093-x.
[48] Kimura Y, Inoue T, Yin F, Tsuzaki K. Inverse Temperature Dependence of Toughness in an Ultrafine Grain-structure Steel. Science 2008;320:1057–60. https://doi.org/10.1126/science.1156084.
[49] Rao KTV, Yu W, Ritchie RO. Cryogenic Toughness of Commercial Aluminum-Lithium Alloys : Role of Delamination Toughening. Met. Trans. 1989;20:485–97.
[50] Alam ME, Pal S, Maloy SA, Odette GR. On Delamination Toughening of a 14YWT Nanostructured Ferritic Alloy. Acta Mater. 2017;136:61–73. https://doi.org/10.1016/j.actamat.2017.06.041.
[51] L. Liu, Q. Yu, Z. Wang, J. Ell, M.X. Huang, R.O. Ritchie, Making Ultrastrong Steel Tough by Grain-boundary Delamination, Science (80-.). 368 (2020) 1347–1352. Doi: 10.1126/science.aba9413.
[52] Arnoult XC, Růžičková M, Kunzová K, Materna A. Short review: Potential Impact of Delamination Cracks on Fracture Toughness of Structural Materials. Frat. Ed Integrita Strutt. 2016;10:509–22. https://doi.org/10.3221/IGF-ESIS.35.57.
[53] T. Tanaka, N. Tabata, T. Hatomura, C. Shiga, Three Stages of the Controlled-Rolling Process, in: Union Carbide Corporation Metals Division (Ed.), Int Symp High Strength Low Alloy Steels, ASTM International, Metals Park, OH, 1977: pp. 107–119.
[54] Shin SY, Hong S, Bae JH, Kim K, Lee S. Separation Phenomenon Occurring During the Charpy Impact Test of API X80 Pipeline Steels. Metall. Mater. Trans. A Phys. Metall. Mater. Sci. 2009;40:2333–49. https://doi.org/10.1007/s11661-009-9943-9.
[55] Yang Z, Huo C, Guo W. The Charpy Notch Impact Test of X70 Pipeline Steel with Delamination Cracks, in. Key Eng. Mater. 2005:2391–6. https://doi.org/10.4028/www.scientific.net/kem.297-300.2391.
[56] Joo MS, Suh D-W, Bae JH, Bhadeshia HKDH. Role of delamination and crystallography on anisotropy of Charpy toughness in API-X80 steel. Mater. Sci. Eng. A. 2012;546:314–22. https://doi.org/10.1016/J.MSEA.2012.03.079.
[57] Yang XL, Xu YB, Tan XD, Wu D. Influences of Crystallography and Delamination on Anisotropy of Charpy Impact Toughness in API X100 Pipeline Steel. Mater. Sci. Eng. A. 2014;607:53–62. https://doi.org/10.1016/j.msea.2014.03.121.
[58] Yang XL, Xu YB, Tan XD, Wu D. Relationships among crystallographic texture, fracture behavior and Charpy impact toughness in API X100 pipeline steel. Mater. Sci. Eng. A. 2015;641:96–106. https://doi.org/10.1016/j.msea.2015.06.029.
[59] Mitchell EB, Lucon E, Collins LE, Clarke AJ, Clarke KD. Microstructure and Thickness Effects on Impact Behavior and Separation Formation in X70 Pipeline Steel. J. Mater. 2020.
[60] E. Mitchell, Toughness And Separation Improvement Of Thick Plate X70 Pipeline Steels, Colorado School of Mines, n.d.
[61] Marigo JJ, Maurini C, Pham K. An Overview of the Modelling of Fracture by Gradient Damage Models. Meccanica 2016;51:3107–28. https://doi.org/10.1007/s11012-016-0538-4.
[62] W. Oldfield, Curve Fitting Impact Test Data: a Statistical Procedure, ASTM Stand. News. 3 (1975) 24–29. https://www.osti.gov/biblio/6253423 (accessed December 9, 2020).
[63] M. Newville, T. Stensitzki, D.B. Allen, M. Rawlik, A. Ingargiola, A. Nelson, M. Newville, T. Stensitzki, D.B. Allen, M. Rawlik, A. Ingargiola, A. Nelson, Lmfit: Non-Linear Least-Square Minimization and Curve-Fitting for Python, Ascl. (2016) ascl:1606.014.
[64] P. Virtanen, R. Gommers, T.E. Oliphant, M. Haberland, T. Reddy, D. Cournapeau, E. Burovski, P. Peterson, W. Weckesser, J. Bright, S.J. van der Walt, M. Brett, J. Wilson, K.J. Millman, N. Mayorov, A.R.J. Nelson, E. Jones, R. Kern, E. Larson, C. Carey, İ. Polat, Y. Feng, E.W. Moore, J. VanderPlas, D. Laxalde, J. Perktold, R. Cimrman, I. Henriksen, E.A. Quintero, C.R. Harris, A.M. Archibald, A.H. Ribeiro, F. Pedregosa, P. van Mulbregt, S. 1. 0 Contributors, SciPy 1.0–Fundamental Algorithms for Scientific Computing in Python, (2019). http://arxiv.org/abs/1907.10121 (accessed January 28, 2020).
[65] F. Di Gioacchino, E. Lucon, E.B. Mitchell, K.D. Clarke, D.K. Matlock, OSF Repository for: Side-grooved Modified Charpy Impact Test to Assess Splitting and Fracture Properties of High-Toughness Plate Steels, (2020). Doi: add DOI.
[66] Morrison WB. Influence of Testing Direction on the Mechanical Properties of Wrought Steel. Met. Technol. 1975;2:33–41. https://doi.org/10.1179/030716975803277636.
[67] Davis BJ. The Effect of Separations on the Assessment of Charpy Impact Tests. Australia: University of Wollongong; 2017.
[68] Van Der Walt S, Schönberger JL, Nunez-Iglesias J, Boulogne F, Warner JD, Yager N, et al. Scikit-image: Image Processing in Python. PeerJ 2014;2014:e453. https://doi.org/10.7717/peerj.453.
[69] Lucon E. Influence of Shear Lip Symmetry on the Fracture Behavior of Charpy Specimens. J. Test. Eval. 2019;47:20180403. https://doi.org/10.1520/JTE20180403.
[70] Yasufumi I, Tomokazu M. Effect of Side Grooves on the Elastic-plastic Stress State of Fracture Toughness Specimens-Three-dimensional Finite Element Analysis. Eng. Fract. Mech. 1982;16:659–68. https://doi.org/10.1016/0013-7944(82)90019-4.
[71] B.L. Bramfitt And, R. Marder, A Study of the Delamination Behavior of a Very Low-Carbon Steel, Metall. Trans. A. 8 (1977) 1263–1273. https://link.springer.com/content/pdf/10.1007%2FBF02643841.pdf (accessed February 2, 2019).
[72] Mintz B, Maina E, Morrison WB. Origin of fissures on fracture surfaces of impact samples of HSLA steels with ferrite/pearlite microstructures. Mater. Sci. Technol. 2007;23:347–54. https://doi.org/10.1179/174328407X161222.
[73] Ashby MF. The Deformation of Plastically Non-homogeneous Materials. Philos. Mag. 1970;21:399–424. https://doi.org/10.1080/14786437008238426.
[74] M. a. Tschopp, B.B. Bartha, W.J. Porter, P.T. Murray, S.B. Fairchild, Microstructure-Dependent Local Strain Behavior in Polycrystals Through In-Situ Scanning Electron Microscope Tensile Experiments, Metall. Mater. Trans. A. 40 (2009) 2363–2368. Doi: 10.1007/s11661-009-9938-6.
[75] Di Gioacchino F, Quinta da Fonseca J. Plastic Strain Mapping with Sub-micron Resolution Using Digital Image Correlation. Exp. Mech. 2013;53. https://doi.org/10.1007/s11340-012-9685-2.
[76] Di Gioacchino F, Quinta Da Fonseca J. An Experimental Study of the Polycrystalline Plasticity of Austenitic Stainless Steel. Int. J. Plast. 2015;74. https://doi.org/10.1016/j.ijplas.2015.05.012.
[77] Edwards TEJ, Di Gioacchino F, Springbett HP, Oliver RA, Clegg WJ. Stable Speckle Patterns for Nano-scale Strain Mapping up to 700 °C. Exp. Mech. 2017;1–14.
[78] Server WL. Instrumented Charpy Test Review and Application to Structural Integrity. Eur. Struct. Integr. Soc. 2002;30:205–12. https://doi.org/10.1016/S1566-1369(02)80022-X.